

Orbital and spin interplay in spin-gap formation in pyroxene ATiSi_2O_6 ($A = \text{Na}, \text{Li}$)

Toshiya Hikihara and Yukitoshi Motome
 RIKEN, 2-1 Hirosawa, Wako, Saitama 351-0198, Japan
 (Dated: March 22, 2024)

Interplay between orbital and spin degrees of freedom is theoretically studied for the phase transition to the spin-singlet state with lattice dimerization in pyroxene titanium oxides ATiSi_2O_6 ($A = \text{Na}, \text{Li}$). For the quasi-one-dimensional spin-1=2 systems, we derive an effective spin-orbital-lattice coupled model in the strong correlation limit with explicitly taking account of the t_{2g} orbital degeneracy, and investigate the model by numerical simulation as well as the mean-field analysis. We find a nontrivial feedback effect between orbital and spin degrees of freedom; as temperature decreases, development of antiferromagnetic spin correlations changes the sign of orbital correlations from antiferro to ferro type, and finally the ferro-type orbital correlations induce the dimerization and the spin-singlet formation. As a result of this interplay, the system undergoes a finite-temperature transition to the spin-dimer and orbital-ferro ordered phase concomitant with the Jahn-Teller lattice distortion. The numerical results for the magnetic susceptibility show a deviation from the Curie-Weiss behavior, and well reproduce the experimental data. The results reveal that the Jahn-Teller energy scale is considerably small and the orbital and spin exchange interactions play a decisive role in the pyroxene titanium oxides.

PACS numbers: 75.30.Et, 75.10.Jm, 75.40.Cx

I. INTRODUCTION

Orbital degree of freedom has attracted much attention since it plays key roles in electronic properties of transition metal compounds.^{1,2} The orbital degree of freedom couples with the Jahn-Teller (JT) lattice distortion, and in many compounds, the energy scale of the JT stabilization energy is larger than that of the spin and orbital exchange interactions.³ A typical example is the mother compound of colossal magnetoresistive (CMR) manganites, LaMnO_3 : The JT energy scale is ~ 0.1 -eV and the spin exchange energy scale is ~ 10 meV. Consequently, the orbital-lattice transition occurs at a much higher temperature (~ 800 K) than the antiferromagnetic (AF) transition temperature (~ 140 K).⁴ In these systems, the orbital-lattice physics is dominant, and the orbital and lattice orderings modify effective spin exchange interactions to lead a magnetic ordering in a secondary effect. Moreover, the JT distortion suppresses fluctuation effects in orbital and spin degrees of freedom. Hence, a large JT coupling masks bare interplay between spin and orbital in many real materials.

Quantum and thermal fluctuations in the competition between the spin and orbital exchange interactions may yield novel phenomena, and therefore, it is highly desired to explore systems in which the genuine spin-orbital interplay appears explicitly. One of promising candidates is the t_{2g} electron system such as titanium and vanadium oxides. In the t_{2g} systems, the JT coupling becomes smaller than in the e_g systems such as CMR manganites because spatial shapes of t_{2g} orbitals avoid directions of surrounding ligands in the octahedral positions. For instance, in vanadium perovskite oxides AVO_3 ($A = \text{La}, \text{Ce}$), the orbital-lattice transition temperature becomes even lower than the AF one,⁵ and novel interplay between spin and orbital is proposed theoretically.^{6,7}

FIG. 1: (a) Lattice structure of pyroxene oxides ATiSi_2O_6 ($A = \text{Na}, \text{Li}$). Chains of TiO_6 octahedra are separated by SiO_4 tetrahedra. (b) Skew edge-sharing chain structure of TiO_6 octahedra. Balls in the center of each octahedron denote Ti cations, and oxygen ions are on the corners of the octahedra. The octahedra share their edges in the xy and yz planes alternatively. White objects with four lobes denote d_{xy} and d_{yz} orbitals of t_{2g} electrons, and t^{11} (t^{22}) is the σ -bond transfer integrals between d_{xy} (d_{yz}) orbitals. See the text for details.

Pyroxene titanium oxides ATiSi_2O_6 ($A = \text{Na}, \text{Li}$) are typical examples of the t_{2g} electron systems where such interplay between spin and orbital is expected.⁸ The lattice structure of these compounds consists of characteristic one-dimensional (1D) chains of skew edge-sharing TiO_6 octahedra as shown in Fig. 1 (a). The TiO_6 chains are bridged and well separated by SiO_4 tetrahedra, and therefore, interchain couplings are considered to be much weaker than intrachain interactions. In each TiO_6 chain, as shown in Fig. 1 (b), the edges of octahedra in the xy and yz planes are alternatively shared between neighboring octahedra, which leads to the zig-zag structure. Each magnetic Ti^{3+} cation has one d electron in these insulating materials. Hence, we may consider that a quasi 1D spin-1=2 system is realized.

Pyroxene titanium oxides show a peculiar phase transition. The magnetic susceptibility shows a sharp drop at $T_c = 210$ K and 230 K in $\text{NaTiSi}_2\text{O}_6$ and $\text{LiTiSi}_2\text{O}_6$, respectively, which indicates the transition to a spin-singlet state with a finite spin gap.⁸ Below T_c , a dimerization of Ti-Ti distances along the chain was observed by the X-ray scattering.⁹ These remind us of a spin-Peierls transition.¹⁰ However, above T_c , the magnetic susceptibility shows an unusual temperature dependence which clearly deviates from that of other spin-Peierls compounds. In spin-Peierls systems, the dimerization

is caused by the magnetoelastic coupling, and therefore, the transition occurs when short-range spin correlations develop enough to drive the lattice dimerization. This development of spin correlations is manifested in a broad peak of the magnetic susceptibility above T_C , and the peak temperature gives a rough estimate of the spin-exchange energy scale. Contrary to this conventional behavior, the magnetic susceptibility of the pyroxene compounds at high temperatures increases as temperature decreases, and suddenly drops at T_C without a clear formation of the broad peak.⁸ This suggests a breakdown of the simple spin-Peierls picture in these pyroxene compounds.

For the peculiar transition to the spin-singlet state, an importance of the t_{2g} orbital degree of freedom has been pointed out.⁸ Theoretically, a scenario of the orbital-driven spin-singlet formation has been explored in spin-orbital coupled models for t_{2g} electron systems.¹¹ It was proposed that the orbital ordering may modify effective spin exchange interactions and induce the spin-singlet formation. However, models were considered only for systems with corner-sharing octahedra, and hence, it is unclear that the argument is applicable to the present pyroxene systems with the edge-sharing octahedra. A similar scenario has been proposed for the present systems,¹² however, the analysis was heuristic and not sufficient to conclude the mechanism of the finite-temperature transition. In order to clarify the nature of the transition and the low-temperature phase, we need more elaborate analysis. In particular, it is indispensable to investigate thermodynamic properties on the basis of a microscopic model.

In the present study, we will theoretically explore the mechanism of the unusual phase transition in the pyroxene titanium oxides ATiSi_2O_6 explicitly taking account of the t_{2g} orbital degree of freedom. We derive an effective spin-orbital-lattice coupled model in the strong correlation limit, and investigate thermodynamics as well as the ground-state properties of the model applying the numerical quantum transfer matrix method and mean-field-type arguments. As a result, we find that interesting interplay between orbital and spin degrees of freedom occurs in the system, and the interplay gives a comprehensive understanding of the peculiar properties of the pyroxene compounds: Although both orbital and spin correlations are antiferro type and compete with each other at high temperatures, development of AF spin correlations with decreasing temperature yields a sign change of orbital correlations from antiferro to ferro type. After the sign change, the ferro-type orbital correlations grow with the antiferro-type spin correlations, and finally, induce the spin-singlet formation with a dimerization. Furthermore, the nontrivial temperature dependence of orbital correlations modifies an effective magnetic coupling, and results in a non-Curie-Weiss behavior of the magnetic susceptibility. We show that our model with realistic parameters reproduces the peculiar temperature dependence of the magnetic susceptibility in experiment.

The organization of this paper is as follows. In the following section II, applying the strong-coupling approach, we derive an effective spin-orbital-lattice coupled model for the t_{2g} pyroxene compounds ATiSi_2O_6 . In Sec. III, we discuss properties of the system in the ground state and in the high-temperature limit using mean-field type arguments. In Sec. IV, we study thermodynamic properties of the effective model by numerical simulations. We describe the method in Sec. IV A. Section IV B shows the numerical results including quantitative comparisons with the experimental data. Finally, Section V is devoted to summary and concluding remarks.

II. MODEL HAMILTONIAN

In this section, we derive an effective spin-orbital-lattice coupled model for the pyroxene oxides ATiSi_2O_6 , whose Hamiltonian reads

$$H = H_{\infty} + H_{JT} + H_{\text{?}} : \quad (1)$$

The first term describes the intersite exchange interactions in spin and orbital degrees of freedom, and the second term includes the Jahn-Teller type orbital-lattice coupling. These two are defined within each 1D chain. The third term describes the interchain coupling.

The spin-orbital exchange Hamiltonian H_{∞} is derived from a t_{2g} multi-orbital Hubbard model by using the perturbation in the strong correlation limit.^{3,13} The skew structure shown in Fig. 1 (b) distorts TiO_6 octahedra in the form that four Ti-O bonds in which the oxygen ions are shared with neighboring TiO_6 octahedra are longer than the rest two Ti-O bonds in each octahedron.⁹ The distortion leads to the splitting of threefold t_{2g} levels into a low-lying doublet with d_{xy} and d_{yz} orbitals and a single d_{zx} level when we take the coordinates as shown in Fig. 1 (b). The splitting is estimated as 300 meV in a pyroxene vanadium oxide which has a similar lattice structure.¹⁴ Because of this level splitting, it is reasonable to start from the 1D Hubbard model with twofold degeneracy of d_{xy} and d_{yz} orbitals with tracing out the higher d_{zx} level. The Hamiltonian is given in the form

$$H_{\text{Hub}} = \sum_{i,j} \sum_{\sigma} t_{ij} c_{i\sigma}^{\dagger} c_{j\sigma} + H_{\text{?}} : \quad (2)$$

$$+ \frac{1}{2} \sum_i \sum_{\sigma} U_{\sigma} c_{i\sigma}^{\dagger} c_{i\sigma} c_{i\sigma}^{\dagger} c_{i\sigma} ;$$

where i, j are site indices within the 1D chain, $\sigma = 0, 1, 2$ are spin indices, and $\sigma = 1$ (d_{xy}) and 2 (d_{yz}) are orbital indices. The first term describes the electron hopping, and the second term denotes the onsite Coulomb interactions where we use the standard parametrizations,

$$U_{\sigma} = U_{\sigma\sigma} = U^0 + J_H (\sigma = 0 + \sigma = 1) ; \quad (3)$$

$$U = U_{11;11} = U_{22;22} = U^0 + 2J_H ; \quad (4)$$

Here, we neglect the relativistic spin-orbit coupling.

The perturbation calculation is performed in the strong correlation limit $t_{ij} \ll U; U^0; J_H$ by taking an atomic eigenstate with one electron at each site. In the edge-sharing configuration as shown in Fig. 1 (b), the most relevant contribution in the transfer integrals t_{ij} is the overlap between the nearest-neighbor (NN) pairs with the same orbitals lying in the same plane, which is called the σ -bond. The σ -bond transfer integrals are $t_{i,i+1}^{11}$ for NN pairs in the xy plane and $t_{i,i+1}^{22}$ for those in the yz plane as shown in Fig. 1 (b). These two types of the transfer integrals take the same value, and we denote them by t in the following. Other transfer integrals are much smaller than t ; in particular, $t_{i,i+1}^{12} = t_{i,i+1}^{21} = 0$ between NN sites from the symmetry. In the present study, we take account of the σ -bond contributions only, and neglect other transfer integrals.¹⁵ The approximation is known to give reasonable results for spinel oxides which also have edge-sharing network of octahedra.¹⁶

The second order perturbation in t gives the effective spin-orbital Hamiltonian in the form

$$H_{so} = \sum_i J (h_{i,i+1}^{oAF} + h_{i,i+1}^{oF}); \quad (5)$$

$$h_{i,i+1}^{oAF} = (A + B S_i \cdot \hat{S}_{i+1}) \frac{1}{2} 2T_i T_{i+1}; \quad (6)$$

$$h_{i,i+1}^{oF} = C \frac{1}{4} S_i \cdot \hat{S}_{i+1} \frac{1}{2} T_i \frac{1}{2} T_{i+1}; \quad (7)$$

where S_i is the $S = 1/2$ spin operator at site i and T_i is the Ising isospin which describes the orbital state at site i as $T_i = +1/2 (-1/2)$ when the d_{xy} (d_{yz}) orbital is occupied. Note that the σ -bond transfer integral t , which is orbital diagonal and does not mix different orbitals, leads to the Ising nature of the orbital isospin interaction. The signs in Eq. (7) take $+$ ($-$) for the bonds within the xy (yz) plane. The coupling constants in Eqs. (5)–(7) are given by parameters in Eq. (2) as

$$J = \frac{(t)^2}{U}; \quad (8)$$

$$A = \frac{3}{4(1-3)} + \frac{1}{4(1-)}; \quad (9)$$

$$B = \frac{1}{1-3} - \frac{1}{1-}; \quad (10)$$

$$C = \frac{4}{3} \frac{1}{1+} + \frac{2}{1-}; \quad (11)$$

$$= \frac{J_H}{U}; \quad (12)$$

where we use Eq. (4). The realistic value of w will be estimated as 0.1 later. Therefore, we consider that A, B , and C are all positive in the following.

We note that a part of the spin-orbital interactions, i.e., $h_{i,i+1}^{oF}$ in Eq. (7) takes a similar form to the model

proposed in Ref. 12. Our model derived from the multi-orbital Hubbard model contains both ferro and anti-ferro types of orbital interactions as well as the nontrivial contributions which are missed in the previous model in Ref. 12. We will show that these factors play important roles in the thermodynamics. We also note that a spin-orbital model similar to Eq. (5) was studied in Ref. 11. The model was derived for the corner-sharing configuration of the octahedra, while our model is for the edge-sharing configuration.

The orbital-lattice coupling term H_{JT} in Eq. (1) is given in the form

$$H_{JT} = \sum_i Q_i T_i + \frac{1}{2} \sum_i Q_i^2; \quad (13)$$

The first term describes the JT coupling where t is the electron-lattice coupling constant and Q_i is the amplitude of the JT distortion which couples to the remaining two-fold degeneracy of the d_{xy} and d_{yz} orbitals. The second term denotes the elastic energy of the JT distortion. For simplicity, we neglect the kinetic energy of phonons and regard Q_i as a classical variable. Here, we note that besides the onsite term there may be intersite interactions of JT distortions such as $\sum_{ij} Q_i Q_j$. However, in the self-consistent scheme described in Sec. IV A, which we will employ in the present numerical study, the intersite interactions do not affect the results except for a shift of the critical temperature. Such effect can be renormalized into the term in Eq. (13), and therefore, we do not explicitly include the intersite term in the present Hamiltonian.

In addition to the above two terms H_{so} and H_{JT} , we also consider the interchain coupling term H_{\perp} in Eq. (1). We may consider two contributions to H_{\perp} . One is the spin-orbital exchange interaction arising from the interchain transfer integrals of electrons, and the other is the interchain interaction of JT distortions. The former is expected to be negligibly small due to a rapid decay and a large spatial anisotropy of the t_{2g} wave functions. We therefore ignore it and take account of the latter JT contribution only. The explicit form of the JT coupling depends on the details of the lattice structure among 1D chains, and may be very complicated. In the present study, we assume the following simple form

$$H_{\perp} = \sum_{\langle i,j \rangle} Q_i Q_j; \quad (14)$$

where the summation is taken over the NN sites in four neighboring chains. Since the TiO_6 chains are well separated by SiO_4 tetrahedra in the pyroxene compounds, the coupling constant t_{\perp} is expected to be small. In the following numerical calculations, we will treat the interchain JT coupling in a mean-field approximation, which is well justified for weakly-coupled 1D systems.¹⁸

Finally, we discuss the realistic values of the parameters. The σ -bond transfer integral is estimated as

t 0.3eV for pyroxene vanadium oxides.⁴ Typical estimates for Coulomb interaction parameters are $U = 5-6$ eV and $\tilde{U} = 0.6-0.7$ eV.¹⁷ Hence, in Eq. (12) is a small parameter of the order of 0.1. From the estimates of t and U , the exchange energy scale J in Eq. (8) is estimated as $J = 200$ K. As for the JT couplings A and B , since there is no experimental estimates to our knowledge, we treat them as parameters which are determined by the comparison between the numerical results and the experimental data in Sec. IV B 2.

III. MEAN-FIELD ANALYSIS

Before going into the numerical study of the thermodynamics of the model (1), we apply mean-field arguments to capture the behavior in the ground state and in the high-temperature phase. For simplicity, we consider only the spin-orbital part H_{so} in this section.

A. Ground state

In the ground state, we here consider four different types of ordered states as shown in Fig. 2 schematically; (a) the spin-ferro and orbital-ferro (sF-oF), (b) the spin-ferro and orbital-antiferro (sF-oAF), (c) the spin-antiferro and orbital-ferro, and (d) the spin-antiferro and orbital-antiferro (sAF-oAF) states. For simplicity, we consider the fully polarized states for the spin-ferro, the orbital-ferro, and the orbital-antiferro orderings, where quantum fluctuations do not play a crucial role. (Note that the orbital isospin is the Ising spin in the present model.) The important point is that as easily shown by Eqs. (6) and (7), the orbital-ferro ordering, i.e., $\langle T_i T_{i+1} \rangle = 1/4$ and $\langle T_i \rangle = 1/2$ (or $-1/2$) for all i , disconnects every other bonds. Hence, when the spin coupling is antiferromagnetic, the orbital-ferro ordering leads to the spin-singlet formation, i.e., $\langle S_i S_{i+1} \rangle = 3/4$ for remaining isolated NN pairs. Therefore, the ordered state (c) is denoted as the spin-dimer and orbital-ferro (sD-oF) state. We note that a similar mechanism of the singlet formation driven by orbital ordering has been proposed for a related model.¹¹

The ground-state energy for each ordered state is calculated by replacing the spin and orbital-isospin operators in Eq. (5) by the following expectation values;

$$\langle S_i S_{i+1} \rangle = \frac{1}{4} \quad \text{for sF pairs}; \quad (15)$$

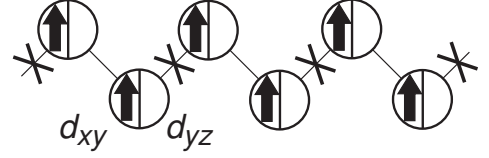
$$\langle S_i S_{i+1} \rangle = \frac{3}{4} \quad \text{for sD pairs}; \quad (16)$$

$$\langle S_i S_{i+1} \rangle = -s \quad \text{for sAF pairs}; \quad (17)$$

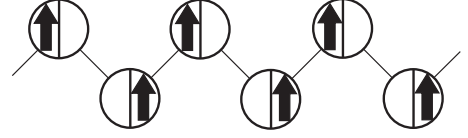
where s is a positive parameter less than $3/4$ (we do not need the precise value of s), and

$$\langle T_i T_{i+1} \rangle = \frac{1}{4}; \quad \langle T_i \rangle = \frac{1}{2} \quad \text{for oF pairs}; \quad (18)$$

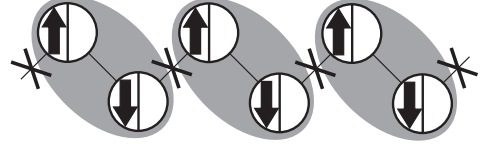
(a) sF-oF



(b) sF-oAF



(c) sD-oF



(d) sAF-oAF

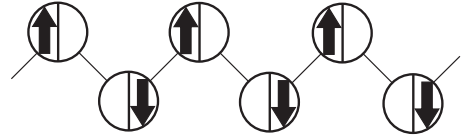


FIG. 2: Spin and orbital ordering patterns in (a) the spin-ferro and orbital-ferro (sF-oF), (b) the spin-ferro and orbital-antiferro (sF-oAF), (c) the spin-dimer and orbital-ferro (sD-oF), and (d) the spin-antiferro and orbital-antiferro (sAF-oAF) states. Circles denote the lattice sites, and two separated spaces inside them denote two different orbital states d_{xy} and d_{yz} as indicated in (a). Arrows denote spins, and gray ovals in (c) represent the spin-singlet pairs. Crosses in (a) and (c) denote the disconnected bonds by the ferro-type orbital ordering. See the text for details.

$$\langle T_i T_{i+1} \rangle = \frac{1}{4}; \quad \langle T_i \rangle = \frac{(-1)^i}{2} \quad \text{for oAF pairs}; \quad (19)$$

respectively. The obtained ground-state energies per site for the states (a)-(d) are

$$E_{\text{sF-oF}} = 0; \quad (20)$$

$$E_{\text{sF-oAF}} = J(A + \frac{B}{4}); \quad (21)$$

$$E_{\text{sD-oF}} = J\frac{C}{2}; \quad (22)$$

$$E_{\text{sAF-oAF}} = J(A - sB); \quad (23)$$

respectively.

We compare Eqs. (20)-(23) by using Eqs. (8)-(11) and obtain

$$(E_{\text{sF-oAF}} \text{ or } E_{\text{sD-oF}}) < E_{\text{sAF-oAF}} < E_{\text{sF-oF}}; \quad (24)$$

Hence, the ground state is either (b) sF-oAF or (c) sD-oF state. From the equation of $E_{\text{sF-oAF}} = E_{\text{sD-oF}}$, we obtain the critical value of γ for the transition between the two phases as

$$\gamma_c = \frac{1}{3} \left(\frac{J}{J_0} - 8 \right), \quad 0 \leq \gamma \leq 8. \quad (25)$$

Namely, we have the ground-state phase transition between the sD-oF and sF-oAF phases by changing γ ; the sD-oF (sF-oAF) phase is stable for $\gamma < \gamma_c$ ($\gamma > \gamma_c$). Hence, for a realistic value of $\gamma \leq 8$, the ground state is predicted to be the sD-oF phase within the mean-field argument. This will be confirmed by the numerical calculations in Sec. IV. We will also show that the sF-oAF state is realized for $\gamma > \gamma_c$ in Appendix B.

The γ -controlled phase transition is understood by the competition between the spin superexchange interaction and the Hund's-rule coupling. The former comes from the perturbation process within the same orbitals and favors the spin-singlet state.¹⁹ The latter enhances the energy gain from the perturbation process between different orbitals and stabilizes the sF-oAF state. It is known that the sF-oAF state is favored by a finite Hund's-rule coupling ($J_H > 0$) in multiorbital systems with transfer integrals $t_{11}^1 = t_{22}^2 \neq 0$ between all the NN sites.^{20,21} In the present systems, the specific form of the transfer integrals due to the zig-zag lattice structure gives a chance to stabilize the sD-oF state in the small γ regime.

B. High-temperature para phase

At high temperatures, both spin and orbital are disordered. We here examine spin and orbital correlations in the para phase by a mean-field type argument.

First, to focus on the spin degree of freedom, we replace the orbital isospin operators in the effective model (5) with their mean values, i.e., $T_i \rightarrow \langle T_i \rangle = 0$ and $T_i T_{i+1} \rightarrow \langle T_i T_{i+1} \rangle = 0$. The resultant effective spin Hamiltonian reads

$$H_s^{\text{MF}} = \sum_i J_{i,i+1}^s S_i \cdot S_{i+1} + K_{i,i+1}^s; \quad (26)$$

where

$$J_{i,i+1}^s = J \frac{1}{4} (C - 2B) + (C + 2B) \langle T_i T_{i+1} \rangle; \quad (27)$$

$$K_{i,i+1}^s = \frac{J}{4} \frac{1}{4} (C + 8A) + (C - 8A) \langle T_i T_{i+1} \rangle; \quad (28)$$

In the high-temperature limit, $\langle T_i T_{i+1} \rangle$ becomes zero and the effective spin exchange constant becomes

$$J_{i,i+1}^s(\gamma \rightarrow 0) = \frac{J}{4} (C - 2B); \quad (29)$$

which is positive for $\gamma \leq 8$ and independent of i . Hence, we end up with a 1D AF spin Heisenberg model.

On the other hand, we can also consider a reduced Hamiltonian for the orbital degree of freedom by replacing the spin operators in the model (5) with their mean values. The result is

$$H_o^{\text{MF}} = \sum_i J_{i,i+1}^o T_i T_{i+1} + L_{i,i+1}^o (T_i + T_{i+1}) + K_{i,i+1}^o; \quad (30)$$

where

$$J_{i,i+1}^o = J \frac{1}{4} \left(\frac{C}{4} + (C + 2B) \langle S_i \cdot S_{i+1} \rangle \right); \quad (31)$$

$$L_{i,i+1}^o = (1) J \frac{C}{2} \frac{1}{4} \langle S_i \cdot S_{i+1} \rangle; \quad (32)$$

$$K_{i,i+1}^o = \frac{J}{4} \left(2A + \frac{C}{4} \right) + (C - 2B) \langle S_i \cdot S_{i+1} \rangle; \quad (33)$$

In the high-temperature limit, $\langle S_i \cdot S_{i+1} \rangle = 0$ and the effective isospin coupling constant becomes

$$J_{i,i+1}^o(\gamma \rightarrow 0) = J \frac{1}{4} \frac{C}{4}; \quad (34)$$

This coupling constant is also positive for $\gamma \leq 8$, and therefore, we obtain a 1D antiferro-type Ising isospin model. [Note that the second term in Eq. (30) cancels out when $\langle S_i \cdot S_{i+1} \rangle = 0$.]

The above arguments indicate that both spin and orbital correlations are antiferro type in the high-temperature limit in our effective model (1). On the contrary, as discussed in Sec. IIIA, the ground state is either the sF-oAF or sD-oF state. This suggests that either spin or orbital correlation has to change from antiferro to ferro type as decreasing temperature. It is implied by Eq. (27) that development of antiferro-type orbital correlations $\langle T_i T_{i+1} \rangle < 0$ may change the sign of $J_{i,i+1}^s$ from positive (antiferro) to negative (ferro). In a similar way, Eq. (31) suggests that development of AF spin correlations $\langle S_i \cdot S_{i+1} \rangle < 0$ may induce the sign change of $J_{i,i+1}^o$. In this manner, the spin and orbital correlations compete with each other. The mean-field-level argument is clearly insufficient to clarify the competition, and we will employ the more powerful numerical analysis in the next section.

IV. NUMERICAL ANALYSIS

A. Method

To study thermodynamic properties of the model (1), we apply the quantum transfer matrix (QTM) method²² combined with the mean-field treatment of the JT distortions. Here, we describe the scheme of our analysis.

Since the present model (1) is highly 1D anisotropic, it is justified to treat the weak interchain coupling H_\perp as

the mean field¹⁸ in the form

$$H_{\text{JT}} = \sum_{\langle ij \rangle} Q_i Q_j = \sum_i z j_i Q_i^2; \quad (35)$$

where Q_j is the mean-field value of the JT distortion at site j and z is the number of NN chains, i.e., $z = 4$ in the present materials. As a result, the total Hamiltonian, $H_{\text{SO}} + H_{\text{JT}} + H_{\text{JT}}$, is reduced to an effective 1D spin-orbital-lattice coupled model in the form

$$\begin{aligned} H &= H_{\text{SO}} + \sum_i Q_i T_i + \frac{1}{2} \sum_i 2z j_i Q_i^2 \\ &= H_{\text{SO}} + \sum_i Q_i T_i + \frac{1}{2} \sum_i Q_i^2; \end{aligned} \quad (36)$$

where the JT coupling and distortion are rescaled as $T_i = \frac{1}{2} 2z j_i$ and $Q_i = \frac{1}{2} 2z j_i Q_i$, respectively. For later use, we define the JT stabilization energy as

$$E_{\text{JT}} = \frac{1}{2} 2z j_i Q_i^2; \quad (37)$$

which is the energy gain by the JT distortion in the absence of H_{SO} .

The optimal values of the JT distortions fQ_i are determined in a self-consistent way. We start from an initial guess of fQ_i and calculate the expectation values of the isospin hT_i by applying the QTM method to the effective 1D model H . Note that the QTM calculation is numerically exact and includes all the fluctuations in spin and orbital degrees of freedom for a given set of fQ_i . See Appendix A for the details of the QTM method. The obtained values of hT_i are used to determine fQ_i self-consistently. The self-consistent equation is obtained by the energy minimization $\partial H / \partial Q_i = 0$ which gives

$$Q_i^{\text{new}} = hT_i; \quad (38)$$

The values of fQ_i^{new} are used as inputs for the next QTM calculation. We iterate the procedure until fQ_i converge to optimal values.

Thermodynamic properties are obtained for the optimal values of fQ_i . We calculate the magnetization per site,

$$m = \frac{1}{L} \sum_i hS_i^z; \quad (39)$$

and the average values of NN spin and orbital correlations,

$$C_s = \frac{1}{L} \sum_i hS_i \cdot S_{i+1}; \quad (40)$$

$$C_o = \frac{1}{L} \sum_i hT_i T_{i+1}; \quad (41)$$

respectively, where L is the length of the chain. We also define the NN spin correlations on odd and even bonds

as

$$C_s^{\text{odd}} = \frac{2}{L} \sum_{i2 \text{ odd}} hS_i \cdot S_{i+1}; \quad (42)$$

$$C_s^{\text{even}} = \frac{2}{L} \sum_{i2 \text{ even}} hS_i \cdot S_{i+1}; \quad (43)$$

respectively, to detect the spin dimerization. See Eqs. (A 6)–(A 10) in Appendix A for the calculation of these quantities. Besides, to calculate the magnetic susceptibility, we perform the calculation within the same framework for the system under the external magnetic field whose Hamiltonian reads

$$H = g \mu_B H \sum_i S_i^z; \quad (44)$$

where g is the g -factor and μ_B is the Bohr magneton, and H is the external magnetic field. The susceptibility is obtained from the numerical derivative of m as

$$\chi = \frac{m(H) - m(0)}{H}; \quad (45)$$

where we use $H = 0.001 \text{ J} = (g \mu_B)$.

The QTM method allows us to treat the system in the thermodynamic limit $L \rightarrow \infty$ directly (see Appendix A). Instead, the results contain a systematic error due to a finite Trotter number M . We need to check carefully the convergence of the results with increasing M . The values of M used in the following calculations are up to $M = 4$ for the case of $\beta = 0$ while up to $M = 3$ for $\beta > 0$. Although these values of M appear to be rather small, we will show that the M -convergence is excellent for the temperature range in the present study, $T > 0.1 \text{ J}$.

B. Results

In this section, we show our numerical results for thermodynamic properties of the model (1) obtained by the method in the previous section. In Sec. IV B 1, we clarify nontrivial feedback effects between orbital and spin degrees of freedom in the absence of the JT coupling. In Sec. IV B 2, we switch on the JT coupling, and compare our numerical results with the experimental data.

1. Interplay between orbital and spin

First, we show our results in the absence of the JT coupling ($\beta = 0$). In this case, the model is reduced to the 1D spin-orbital model H_{SO} [Eq. (5)], and we can obtain thermodynamic properties by performing the QTM calculation without any self-consistent iteration.

Figure 3 shows the results of the magnetic susceptibility in Eq. (45) for several values of β . Note that the results for different values of the Trotter number $M = 2, 3$, and 4 almost coincide with each other as shown in the

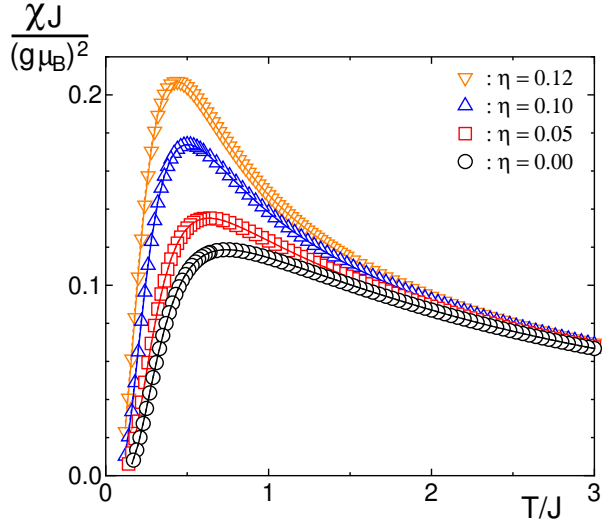


FIG. 3: Temperature dependence of the magnetic susceptibility for $\eta = 0.0; 0.05; 0.10$, and 0.12 . Symbols represent the results for $M = 4$ while solid and dotted curves are those for $M = 3$ and $M = 2$, respectively.

figure, which ensures the convergence of the QTM results in this parameter range. The magnetic susceptibility at high temperatures increases as temperature decreases, and exhibits a broad peak at some temperature. At lower temperatures, it decays rapidly and approaches zero as $T \rightarrow 0$. While the peak becomes sharper and shifts to a lower temperature region as η increases, the rapid decay of χ at low temperatures is commonly observed. This indicates that our spin-orbital model H_{so} in Eq. (5) exhibits the spin-singlet ground state in the small regime as predicted in Sec. III A. (See Appendix B for the larger regime.)

To clarify the nature of the system in more detail, in Fig. 4, we show the results of NN spin and orbital correlations C_s and C_o defined in Eqs. (40) and (41), respectively. The M -dependence of the results is negligible also for these quantities. We note that at finite temperatures no true long-range order appears in the 1D spin-orbital model H_{so} , and hence the NN spin correlations are uniform, i.e., $C_s = C_s^{\text{odd}} = C_s^{\text{even}}$. As $T \rightarrow 0$, the spin and orbital correlations converge to $C_s = 3/8$ and $C_o = 1/4$, respectively. These are indeed the values expected in the sD-oF ground state shown in Fig. 2 (c), where $\langle \mathbf{S}_i \cdot \mathbf{S}_{i+1} \rangle$ takes the value of $3/4$ or 0 alternatively from bond to bond while $\langle \mathbf{T}_i^z \mathbf{T}_{i+1}^z \rangle = 1/4$ for all bonds. Hence, we conclude that the ground state of the system is the sD-oF state in Fig. 2 (c) for the realistic values of $\eta \leq 0.1$, and the rapid decay of χ at low temperatures in Fig. 3 is due to the spin-singlet formation in the ground state.

Let us examine the finite-temperature behavior of C_s and C_o in Fig. 4. At high temperatures, both the spin and orbital correlations are negative, i.e., antiferro type, being consistent with the mean-field prediction in Sec. III B. Here, the spin and orbital antiferro correlations compete

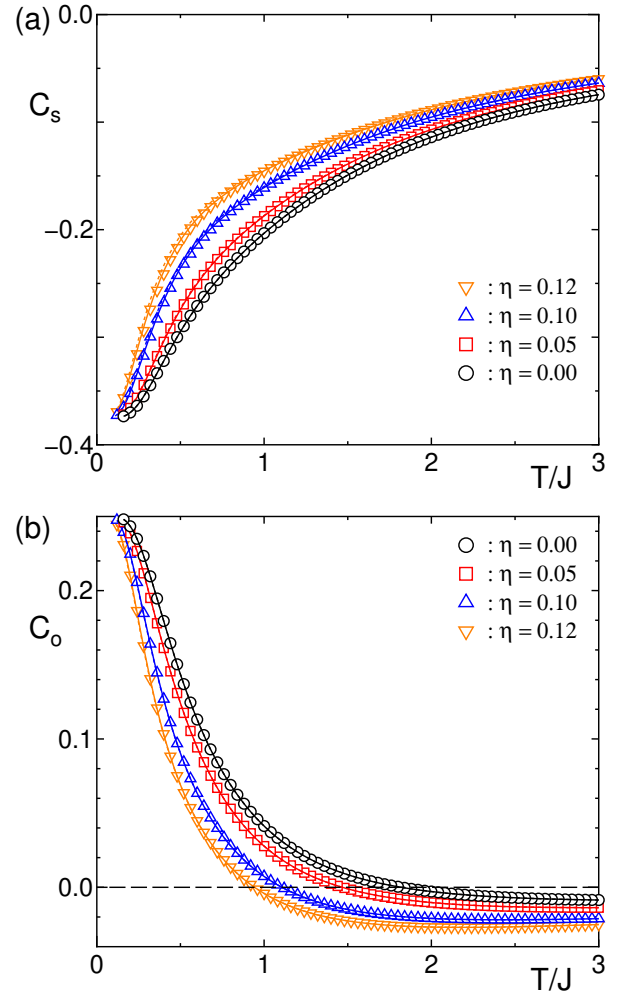


FIG. 4: Temperature dependences of (a) the nearest-neighbor spin correlation C_s and (b) the nearest-neighbor orbital correlation C_o for $\eta = 0.0; 0.05; 0.10$, and 0.12 . Symbols represent the results for $M = 4$ while solid and dotted curves are those for $M = 3$ and $M = 2$, respectively.

with each other since the spin-antiferro correlation favors the orbital-ferro one and vice versa as indicated in the form of H_{so} in Eq. (5). We find that in this range of η the spin-antiferro correlation grows more rapidly than the orbital correlation as T decreases. This growth of C_s suppresses C_o and causes the sign change of C_o from antiferro to ferro type. Once C_o becomes ferro type, C_s and C_o develop cooperatively, and eventually the ferro-type orbital correlation induces the spin-dimer formation in the ground state. These results clearly indicate that our model H_{so} shows a nontrivial feedback effect between orbital and spin degrees of freedom at finite temperatures.

The strong interplay between orbital and spin also shows up in the temperature dependence of the magnetic susceptibility at high temperatures. There, we expect a deviation from the Curie-Weiss behavior due to the interplay since $J_{i,i+1}^s$ depends on the NN orbital correlation

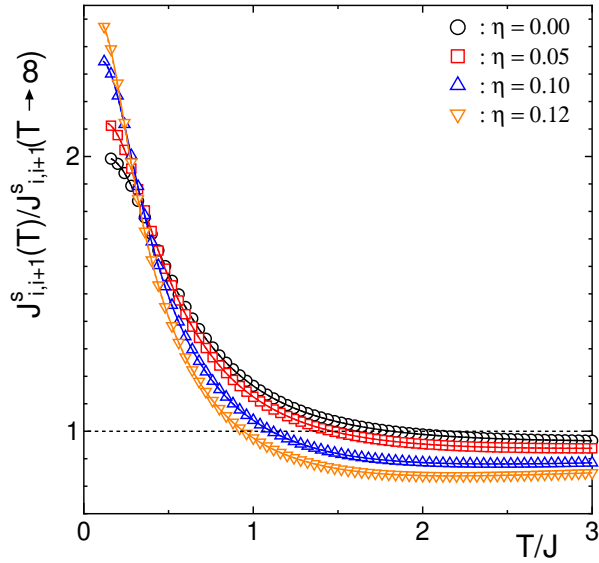


FIG. 5: Effective spin exchange coupling $J_{i,i+1}^s$ in Eq. (27) for $\eta = 0.0; 0.05; 0.10$, and 0.12 . The results are scaled by their values in the high-temperature limit, $J_{i,i+1}^s(T \rightarrow \infty)$.

$hT_{i,i+1}$ as mentioned in Sec. IIIB. The deviation can be monitored by the temperature dependence of the effective spin exchange coupling $J_{i,i+1}^s$ in Eq. (27), since it gives an effective Curie-Weiss temperature θ_{CW} . (In the mean-field approximation, $\theta_{CW} = J_{i,i+1}^s/2$ in the 1D spin-1=2 system with NN interaction.)

In Fig. 5, we show the temperature dependence of $J_{i,i+1}^s$ in Eq. (27) scaled by the value in the high-temperature limit. The results clearly show that $J_{i,i+1}^s$ is temperature-dependent even in the temperature range where the Curie-Weiss fitting to the experimental data has been attempted in Ref. 8. (The energy scale of J will be estimated as 200–300K from the fitting in the next section.) We need further careful considerations in the fitting of the experimental data of the magnetic susceptibility to estimate the model parameters.

2. Comparison with experimental results

Next, we show our results in the presence of the JT coupling, i.e., for the case of $\eta > 0$ in Eq. (36), and compare them with experimental data quantitatively. The numerical results shown in the following are obtained from the self-consistent iteration of the QTM calculation with $M = 3$, and we have confirmed the M -convergence of the results.

Figure 6 shows the results of the magnetic susceptibility χ . The results show a singularity at some temperature and a sudden drop below there, which corresponds to the phase transition to the low-temperature SDOF phase as discussed later. For comparison, we plot the experimental data for $\text{NaTiSi}_2\text{O}_6$,²³ which increase as T de-

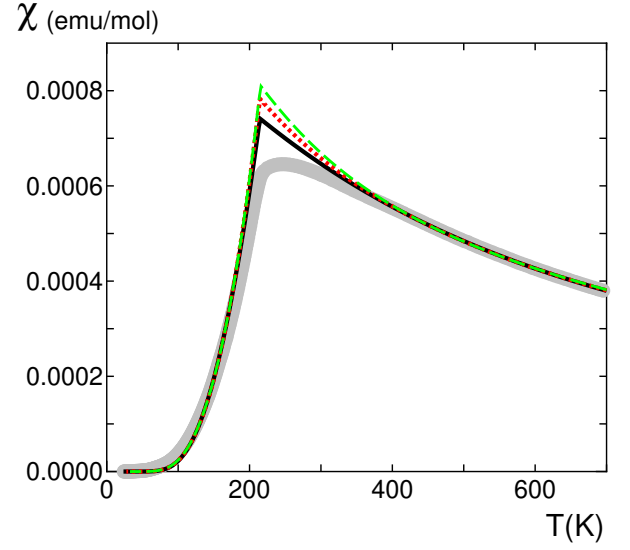


FIG. 6: Comparison between numerical and experimental results of the magnetic susceptibility χ . Solid, dotted, and dashed curves represent the numerical results for $(J; g; J_T) = (213\text{K}; 0.05; 1.85; 86\text{K})$, $(250\text{K}; 0.10; 1.87; 90\text{K})$, and $(296\text{K}; 0.12; 1.90; 89\text{K})$, respectively. Bold gray curve represents the experimental data in Ref. 8.

creases at high temperatures and exhibit a sharp drop at $T_c = 210\text{K}$. The numerical results are obtained for several typical parameter sets estimated by the following fitting procedure: In our model, there are four parameters, i.e., the effective exchange coupling J , the ratio of Coulomb interactions $\eta = J_H/U$, the g -factor g , and the JT coupling parameter J_T . For a certain value of η , we perform the two-parameter fitting by using J and g in the high-temperature regime of $400\text{K} < T < 700\text{K}$, where the JT coupling is irrelevant in the present scheme of the calculation. Using the optimal values of J and g , we determine to reproduce the critical temperature $T_c = 210\text{K}$. We thereby obtain the optimal set of J , g , and J_T for a certain value of η .

In Fig. 6, we show the results of the fitting for $\eta = 0.05; 0.10$, and 0.12 as typical examples. The estimates of the parameters are $(J; g; J_T) = (213\text{K}; 1.85; 86\text{K})$, $(250\text{K}; 1.87; 90\text{K})$, and $(296\text{K}; 1.90; 89\text{K})$ for $\eta = 0.05$, 0.10 , and 0.12 , respectively. As shown in the figure, the numerical results well reproduce the experimental data, except for a small deviation near T_c (discussed below). Although we cannot determine the best set of the parameter values only from the present fitting, we find that the estimates are quite reasonable in this t_{2g} compound: The estimates of J 200–300K are comparable to the estimate based on microscopic parameters in Sec. II. As for the g -factor, although there is no estimate for the present compound as far as we know, it is known that g becomes slightly smaller than two in some t_{2g} compounds,^{24,25} and therefore we believe that our estimates of g are reasonable. Furthermore, the estimates of $J_T \sim 90\text{K}$, which

are smaller than the exchange energy J , also appear to be reasonable for t_{2g} electron systems. (We will comment on the magnitude of J_{JT} in the end of this section.) Therefore, we believe that our effective model (1) with realistic parameters can describe successfully the peculiar properties of the pyroxene compound $\text{NaTiSi}_2\text{O}_6$.

We note that the small deviation near T_c can be attributed to the approximation in the treatment of the JT distortion Q_1 : Our method to determine Q_1 is not able to include effects of the short-range correlations and thermal fluctuations of lattice distortions, which tend to enhance the spin-singlet fluctuation and suppress the magnetic susceptibility. It is therefore reasonable that our method overestimates around the critical point, where the effects become significant. We believe that better agreement near T_c may be obtained by including such effects, however this interesting problem is left for further study.

As shown in Fig. 6, the magnetic susceptibility of our model shows an exponential decay at low temperatures well below T_c . We estimate the spin gap Δ_s from the results below $0.5T_c$ by the fitting function

$$\chi \sim \exp(-\Delta_s/T). \quad (46)$$

The estimates of Δ_s are 665, 640, and 638 K for $\Delta_{JT} = 0.05, 0.10$, and 0.12 , respectively. In experiment, the spin gap Δ_s is estimated as 500 K⁸, which is comparable to our numerical results.

Next, we show the results of the spin and orbital correlations in Fig. 7. Here, we plot only the results for the parameter set of $(J; \Delta_{JT}) = (250 \text{ K}; 90 \text{ K})$ as a typical example since essentially the same behavior is obtained for other parameter sets in Fig. 6.²⁶ The correlations take the same values as those for $\Delta_{JT} = 0$ above T_c . Below T_c , the NN spin correlations on odd and even bonds, C_s^{odd} and C_s^{even} , take different values and converge to $\pm 1/4$ or 0 as $T \rightarrow 0$. This indicates that the translational symmetry is broken in the spin-dimer phase. (Note that one of the doubly-degenerate ordered states is selected depending on the initial set of fQ_{ij} used in the self-consistent calculation.) On the other hand, the NN orbital correlation C_o is uniform, and goes to the value of $1/4$ as $T \rightarrow 0$. As shown in the inset of Fig. 7 (b), the isospin polarization $\langle T_{ij} \rangle$ becomes finite below T_c , indicating the long-range orbital ordering. These results explicitly show that the system below T_c is in the SD phase in Fig. 2 (c).

In Fig. 8, we plot the effective spin exchange coupling J_{ij+1}^s , corresponding to Eq. (27) in the case of $\Delta_{JT} = 0$. For a finite Δ_{JT} , we have to keep the linear terms of $\langle T_{ij} \rangle$ in the reduced spin Hamiltonian in Eq. (26), which give rise to an additional term $-J(\frac{1}{2}C = 2(\langle T_{ij} \rangle + \langle T_{i+1,j} \rangle))$ to J_{ij+1}^s in Eq. (27). As shown in Fig. 8, the value of J_{ij+1}^s deviates from that for $\Delta_{JT} = 0$ below T_c , and takes two alternative values from bond to bond. This clearly shows the alternating behavior of the magnetic coupling in the spin-dimer state. At low temperatures $T < 150 \text{ K}$, the dimerization is almost perfect, i.e., J_{ij+1}^s on the weak

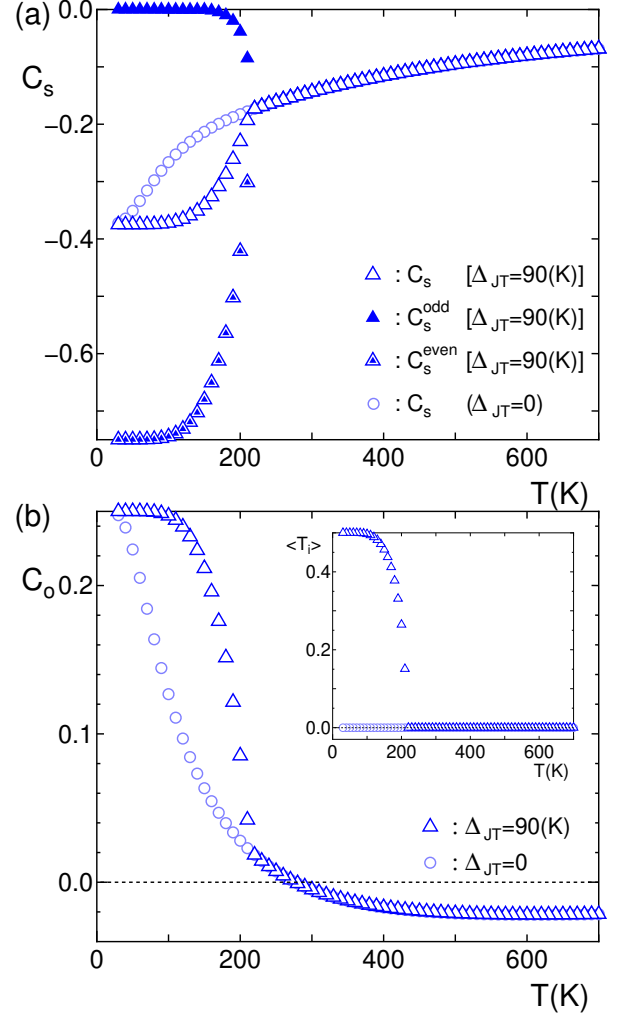


FIG. 7: Temperature dependences of (a) the nearest-neighbor spin correlations C_s , C_s^{odd} , and C_s^{even} , and (b) the nearest-neighbor orbital correlation C_o for $(J; \Delta_{JT}) = (250 \text{ K}; 90 \text{ K})$. Circles show the data for $\Delta_{JT} = 0$ for comparison. Inset in (b): Polarization of orbital isospin.

bonds are almost zero. Hence, there the system consists of almost independent spin-singlet pairs. Note that J_{ij+1}^s on the strong bonds is surprisingly enhanced up to 1000 K. The almost perfect dimerization and the enhanced exchange coupling are the unique aspects of the present spin-orbital-lattice coupled system.

Our estimates of the JT stabilization energy Δ_{JT} 90 K are considerably smaller than $T_c = 210 \text{ K}$ as well as $J = 200 - 300 \text{ K}$. This suggests that the critical temperature T_c is not determined mainly by the JT coupling, and that the balance of the JT coupling and the spin-orbital intersite interaction is important in this t_{2g} electron system. Moreover, we note that the phase transition occurs below the temperature where the orbital correlation C_o changes its sign from negative (antiferro type) to positive (ferro type) as shown in Fig. 7 (b). This indicates an importance of the interplay and the feedback effect be-

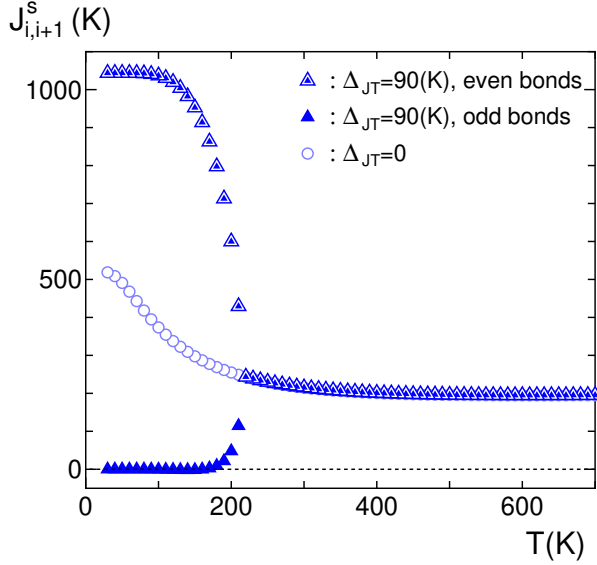


FIG. 8: Temperature dependence of the effective spin-exchange coupling $J_{i,i+1}^s$ for $(J; \Delta_{JT}) = (250\text{K}; 0; 90\text{K})$. Circles show the data for $\Delta_{JT} = 0$ for comparison.

tween spin and orbital in the present system. Therefore, we conclude that the pyroxene compounds are typical t_{2g} electron systems where the JT energy scale is relatively small and the bare interplay between spin and orbital degrees of freedom plays a central role in the thermodynamic properties.

V. SUMMARY AND CONCLUDING REMARKS

In this paper, we have studied the effective spin-orbital-lattice coupled model which we derived to understand the peculiar phase transition to the spin-singlet state in ATiSi_2O_6 ($A = \text{Na}, \text{Li}$). Using the mean-field-type analysis and the numerical quantum transfer matrix method, we have clarified that the interplay between spin and orbital degrees of freedom plays a central role in thermodynamic properties of the system. At high temperatures, both spin and orbital correlations are antiferro type and compete with each other. As temperature decreases, the antiferromagnetic spin correlation grows rapidly and yields the sign change of the orbital correlation from antiferro to ferro type so that the frustration is released. This ferro-type orbital correlation with the Jahn-Teller coupling finally causes a transition to the spin-dimer and orbital-ferro ordered phase. The feedback effect between orbital and spin degrees of freedom results in peculiar temperature dependence of the magnetic susceptibility. We have shown that the magnetic susceptibility data for $\text{NaTiSi}_2\text{O}_6$ can be explained by our effective model with realistic values of parameters.

The transition to the spin-singlet state in the present system shows several different aspects from conventional

spin-Peierls systems. One is the temperature dependence of the magnetic susceptibility. In the present system, the rapid decay of the susceptibility due to the spin-singlet formation occurs even without a broad peak as a fingerprint of well-developed spin correlations. This is because the driving force of the transition is not the magnetoelastic interaction but the orbital-ferro correlations assisted by the Jahn-Teller distortion. However, this does not mean that the orbital-lattice physics is dominant as in e_g electron systems such as CMR manganites. In the present t_{2g} electron system, the Jahn-Teller energy scale is considerably smaller than the orbital and spin exchange interactions, and the orbital-ferro correlation is induced by the keen competition between the orbital and spin degrees of freedom. These illuminate a unique feature of the present t_{2g} system, namely, there the interplay between orbital and spin appears explicitly without being dominated by Jahn-Teller physics.

Another peculiar aspect of the spin-dimer state in our model is that the spin-singlet pairs are formed on the longer Ti-Ti bonds rather than the shorter ones. In the present system, say, the d_{xy} orbital ordering is concomitant with the flattening of TiO_6 octahedra in the z direction which elongates Ti-Ti bonds in the xy plane. Since the spin exchange interaction is strong between the nearest-neighbor sites in the xy plane in this d_{xy} ordered state, the spin-singlet dimers are formed on the longer Ti-Ti bonds. This aspect is clearly different from the conventional spin-Peierls systems in which the spin-singlet pairs are on shorter bonds. In our model, however, we take account of only the tetragonal Jahn-Teller mode which couples to d_{xy} and d_{yz} orbitals. For detailed comparisons with the experimental data which show much complicated lattice structure at low temperatures, it is necessary to include more general lattice distortions in our theory. In particular, we note that the magnetoelastic coupling can be substantial in the low-temperature orbital-ordered phase since the orbital-ferro ordering largely enhances the effective spin exchange coupling on strong bonds up to 1000K as shown in Sec. IV B 2. The magnetoelastic coupling will cause an opposite effect on the Ti-Ti bond lengths since it tends to shorten the spin-singlet Ti-Ti bonds. Further study is necessary to conclude the low-temperature lattice structure. Note that the inclusion of such magnetoelastic effect does not alter our conclusions on the mechanism of the phase transition because it becomes important only when the orbital-ferro ordering is well established far below the critical temperature.

In the present study, we have compared our results of the magnetic susceptibility with the experimental data for the Na compound $\text{NaTiSi}_2\text{O}_6$. There is another compound in this pyroxene family, i.e., $\text{LiTiSi}_2\text{O}_6$. The Li compound also shows the phase transition at $T_c = 230\text{K}$ showing a sudden decay of the magnetic susceptibility below T_c .⁸ However, the susceptibility data show some extra anomalies probably due to impurity phases. We believe that our model describes essential physics in both

the Na and Li compounds. Further experimental study including the sample refinement is desired to compare the data of Li compounds to our results.

As shown in Sec. III A and in Appendix B, the low-temperature phase of our effective model turns into the spin-ferro and orbital-antiferro ordered state for larger values of α than the critical value of $\alpha_c \approx 0.18$. The parameter α is the ratio of the Hund's-rule coupling to the intraorbital Coulomb repulsion, and is considered to be $0.1 < \alpha$ in the present compounds. Unfortunately, it is difficult to control the parameter α experimentally, however, it may vary for different compounds to some extent. If α becomes close to α_c in some compound, there would occur interesting phenomena related to the criticality of the phase transition at α_c . One interesting example is the phase transition from the spin-dimer and orbital-ferro state to the spin-ferro and orbital-antiferro state by applying the external magnetic field. We have investigated this issue in our effective model, and indeed observed the field-induced phase transition. The results will be reported elsewhere. The experimental study of this issue is left for future study.

Acknowledgments

We would like to thank M. Isobe for useful discussions and providing us the experimental data. We also appreciate H. Seo for valuable comments and drawing our attention to the present problem in the early stage of the study. This work is supported by NAREG IN anoscience Project.

APPENDIX A: QUANTUM TRANSFER MATRIX METHOD

In this appendix, we briefly review the algorithm of the QTM method.²² The QTM calculation is applied to the effective 1D model (36) in the self-consistent scheme as described in Sec. IV A.

After the Suzuki-Trotter decomposition, the partition function is represented in terms of the transfer matrix as

$$Z = \text{Tr} e^{-H} = \lim_{M \rightarrow \infty} \text{Tr} T_M^{L=2M} \quad (\text{A } 1)$$

where $\beta = 1/T$ (we set the Boltzmann constant $k_B = 1$), M is the Trotter number, and L is the system size. The transfer matrix T_M is given by

$$T_M = e^{-\tilde{H}_{2n-1;2n} M} e^{-\tilde{H}_{2n;2n+1} M} \quad (\text{A } 2)$$

where \tilde{H} is decomposed into the summation of the local Hamiltonian $\tilde{H}_{i;i+1}$ for bond $(i; i+1)$. We omitted the index n on the transfer matrix T_M since T_M for the present system is invariant under the two-site translation.

The advantage of the QTM method is that we can calculate thermodynamic quantities directly from the largest eigenvalue λ_{\max} and the corresponding right \mathbf{y}^r and left \mathbf{y}^l eigenvectors of T_M .²⁷ (Note that the eigenvectors \mathbf{y}^r and \mathbf{y}^l are different in general since T_M is an asymmetric matrix.) The partition function of the infinite system is found to be $Z = \lim_{L \rightarrow \infty} \lambda_{\max}^{L/2}$, and consequently, the free energy per site can be obtained as

$$f = \frac{1}{2} \ln \lambda_{\max} \quad (\text{A } 3)$$

Hence, once the value of λ_{\max} is obtained, we can calculate any bulk quantity in the thermodynamic limit by taking the appropriate derivative of the free energy f .

Furthermore, we can calculate expectation values of site and bond operators.²⁸ For instance, an expectation value of a product of operators $O_{2n-1;2n} O_{2n;2n+1}$ defined at sites $(2n-1; 2n; 2n+1)$ is obtained from the formula

$$\langle O_{2n-1;2n} O_{2n;2n+1} \rangle = \lim_{M \rightarrow \infty} \frac{\mathbf{y}^l T_M^O \mathbf{y}^r}{\lambda_{\max}}; \quad (\text{A } 4)$$

where

$$T_M^O = O_{2n-1;2n} O_{2n;2n+1} T_M \quad (\text{A } 5)$$

In the present study, we diagonalize the transfer matrix T_M numerically using the simple power method, which is known to be stable in the diagonalization of asymmetric matrix.²⁹ Then, using Eqs. (A 4) and (A 5), we calculate the magnetization m [Eq. (39)] and the NN spin and orbital correlations C_s and C_o [Eqs. (40) and (41)] by

$$m = \frac{\langle S_{2n-1}^z + S_{2n}^z \rangle}{2}; \quad (\text{A } 6)$$

$$C_s = \frac{\langle S_{2n-1} S_n + S_{2n} S_{n+1} \rangle}{2}; \quad (\text{A } 7)$$

$$C_o = \frac{\langle T_{2n-1} T_{2n} + T_{2n} T_{2n+1} \rangle}{2}; \quad (\text{A } 8)$$

respectively. The NN spin correlations on odd and even bonds [Eqs. (42) and (43)] are given by

$$C_s^{\text{odd}} = \langle S_{2n-1} S_n \rangle; \quad (\text{A } 9)$$

$$C_s^{\text{even}} = \langle S_{2n} S_{n+1} \rangle; \quad (\text{A } 10)$$

respectively. In the spin-dimer phase, C_s^{odd} and C_s^{even} may take different values.

APPENDIX B: TRANSITION TO SPIN-F AND ORBITAL-AF PHASE

In this appendix, we discuss thermodynamic properties of the model (1) for larger values of α than those studied in Sec. IV B. There, the sF-oAF ground state is expected to be stable from the mean-field-type analysis in Sec. III A.

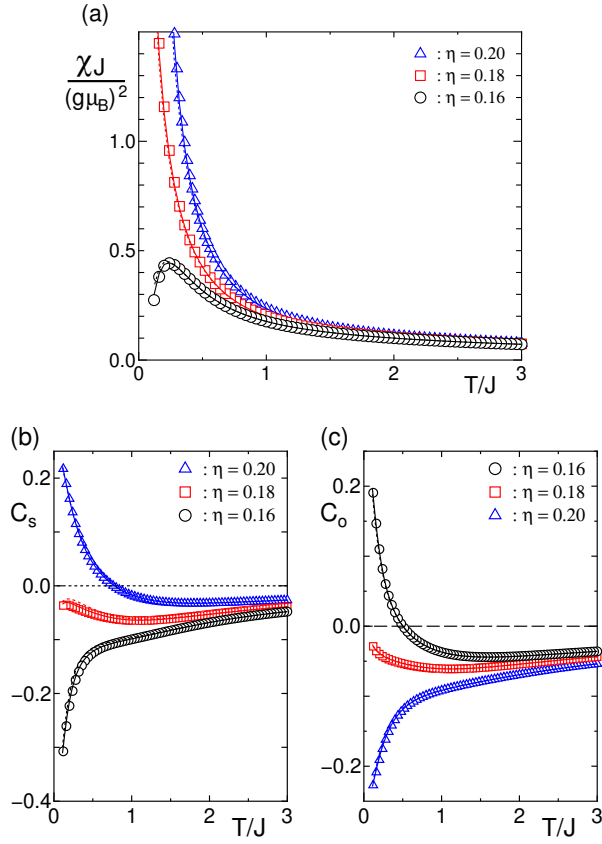


FIG. 9: Temperature dependences of (a) the magnetic susceptibility χ , (b) the nearest-neighbor spin correlation C_s , and (c) the nearest-neighbor orbital correlation C_o for $\eta = 0.16; 0.18$ and 0.20 . Symbols represent the results for $M = 4$ while solid and dotted curves are those for $M = 3$ and $M = 2$, respectively.

We first discuss our numerical results for the spin-

orbital model H_{so} , i.e., the effective model (36) without the JT coupling $\lambda = 0$, corresponding to the results in Sec. IV B 1. Figure 9 (a) shows the results of the magnetic susceptibility. The result for $\eta = 0.16$ exhibits a sharp drop as $T \rightarrow 0$ similarly to the results in Fig. 3, indicating the spin-singlet ground state. On the contrary, for $\eta = 0.18$ and 0.20 , exhibits a divergent behavior as $T \rightarrow 0$, suggesting that the ground state is magnetic. These suggest that there is a ground-state phase transition between nonmagnetic and magnetic phases at $\eta_c \approx 0.18$.

To clarify the nature of the transition in more detail, we show the results of NN spin and orbital correlations C_s and C_o in Figs. 9 (b) and (c), respectively. The results for $\eta = 0.16$ show similar features to those for smaller η shown in Sec. IV B, and indicate that the system exhibits the sD-oF ground state. For $\eta = 0.20$, on the other hand, the antiferro-type orbital correlation C_o develops rapidly, yielding the sign change of the spin correlation C_s . After the sign change, the two correlations grow cooperatively, and approach the values of $C_s = 1/4$ and $C_o = -1/4$ as $T \rightarrow 0$. These are the values expected in the sF-oAF ground state shown in Fig. 2 (b). Hence, the system with $\eta = 0.20$ exhibits the sF-oAF ground state. For $\eta = 0.18$, C_s and C_o are both antiferro type and compete with each other down to the lowest temperature studied here. This suggests that $\eta = 0.18$ is close to the phase boundary between the sD-oF and sF-oAF phases. Therefore, we conclude that the ground state of the spin-orbital model H_{so} undergoes a phase transition between the sD-oF and sF-oAF phases at $\eta_c \approx 0.18$. The critical value is in good agreement with the mean-field prediction in Sec. III A.

In the case of a finite JT coupling, we have found that there occurs a finite-temperature phase transition to the low-temperature sF-oAF phase for $\eta > \eta_c$ or to the sD-oF phase for $\eta < \eta_c$. The details will be reported elsewhere.

¹ Y. Tokura and N. Nagaosa, *Science* **288**, 462 (2000).
² M. Imada, A. Fujimori, and Y. Tokura, *Rev. Mod. Phys.* **70**, 1039 (1998).
³ K. I. Kugel and D. I. Khomskii, *Sov. Phys. Usp.* **25**, 231 (1982).
⁴ E. O. Wollan and W. C. Koehler, *Phys. Rev.* **100**, 545 (1955); J. B. Goodenough, *Phys. Rev.* **100**, 564 (1955).
⁵ S. Miyasaka, Y. Okimoto, M. Iwama, and Y. Tokura, *Phys. Rev. B* **68**, 100406(R) (2003).
⁶ Y. Motome, H. Seo, Z. Fang, and N. Nagaosa, *Phys. Rev. Lett.* **90**, 146602 (2003).
⁷ G. Khalullin, P. Horsch, and A. M. Oleś, *Phys. Rev. Lett.* **86**, 3879 (2001).
⁸ M. Isobe, E. Nishimura, A. Vasil'ev, and Y. Ueda, *J. Phys. Soc. Jpn.* **71**, 1423 (2002).
⁹ E. Nishimura, M. Isobe, Y. Ueda, M. Nishi, K. Ohoyama, H. Sawa, and T. Ohama, *Physica B* **329-333**, 884 (2003).
¹⁰ J. W. Bray, L. V. Interrante, I. S. Jacobs, J. C. Bonner, *Extended Linear Chain Compounds vol. 3*, ed. by J. C. Miller

(New York, Plenum Press, 1983) p. 353; J. P. Boucher and L. P. Regnault, *J. Phys. I (France)* **6**, 1939 (1996); K. Uchinkura, *J. Phys. Condens. Matter* **14**, 195 (2002).
¹¹ N. Katoh, *J. Phys. Soc. Jpn.* **68**, 258 (1999).
¹² M. J. Konstantinovic, J. van den Brink, Z. V. Popovic, V. V. Moschchalkov, M. Isobe, and Y. Ueda, *Phys. Rev. B* **69**, 020409(R) (2004).
¹³ K. I. Kugel and D. I. Khomskii, *Sov. Phys. Solid. State* **17**, 285 (1975).
¹⁴ P. Millet, F. Mila, F. C. Zhang, M. Mambrini, A. B. Van Oosten, V. A. Pashchenko, A. Sulpice, and A. Stepanov, *Phys. Rev. Lett.* **83**, 4176 (1999).
¹⁵ We note that the transfer integrals may be modified by the JT distortion. We neglect the small corrections in the present study.
¹⁶ H. Tsunetsugu and Y. Motome, *Phys. Rev. B* **68**, 060405(R) (2003); Y. Motome and H. Tsunetsugu, preprint (cond-mat/0406039), to be published in *Phys. Rev. B*.
¹⁷ T. Mizokawa and A. Fujimori, *Phys. Rev. B* **54**, 5368

- (1996).
- ¹⁸ Y. Imry, P. Pincus, and D. Scalapino, *Phys. Rev. B* **12**, 1978 (1975); H. J. Schulz, *Phys. Rev. Lett.* **77**, 2790 (1996).
 - ¹⁹ P. W. Anderson, *Phys. Rev.* **115**, 2 (1959).
 - ²⁰ L. M. Roth, *Phys. Rev.* **149**, 306 (1966).
 - ²¹ S. Inagaki and R. Kubo, *Int. J. Magnetism* **4**, 139 (1973); S. Inagaki, *J. Phys. Soc. Jpn.* **39**, 596 (1975).
 - ²² H. Betsuyaku, *Phys. Rev. Lett.* **53**, 629 (1984); *Prog. Theor. Phys.* **73**, 319 (1985).
 - ²³ The experimental data shown in Fig. 6 correspond to χ_m in Ref. 8 which contain only the intrinsic contributions after the subtractions of a Curie contribution from magnetic impurities and a constant term due to core-electron diamagnetism and the Van Vleck paramagnetism.
 - ²⁴ V. Kataev, J. Baier, A. Moller, L. Jongen, G. Meyer, and A. Freimuth, *Phys. Rev. B* **68**, 140405(R) (2003).
 - ²⁵ I. Yamada, H. Manaka, H. Sawa, M. Nishi, M. Isobe, and Y. Ueda, *J. Phys. Soc. Jpn.* **67**, 4269 (1998).
 - ²⁶ Note that the results of the correlations are independent of the value of g .
 - ²⁷ M. Suzuki and M. Inoue, *Prog. Theor. Phys.* **78**, 787 (1987); M. Inoue and M. Suzuki, *Prog. Theor. Phys.* **79**, 645 (1988).
 - ²⁸ X. Wang and T. Xiang, *Phys. Rev. B* **56**, 5061 (1997).
 - ²⁹ E. Carlson, M. Henkel, and U. Schollwöck, *Eur. Phys. J. B* **12**, 99 (1999).

This figure "fig1.jpg" is available in "jpg" format from:

<http://arxiv.org/ps/cond-mat/0404730v2>